Journal of Space Science and Technology

P-ISSN: 2008-4560
E-ISSN: 2423-4516

Vol. VV, No. V, pp.1-17, 2026
https://doi.org/10.22034/jsst.2026.1561
Journal Homepage: https://jsstpub.com

Original Research Paper

Optimized Type 2 Neuro-Fuzzy Control for Robust Orbital Maneuvers under Hall-Effect Thruster Faults and Uncertainty

Mahdi Mansoury[1], Sehraneh Ghaemi[2*], Samira Mir Mazhari Anvar[3] and, Morteza Farhid[4]

1,2. Faculty of Electrical and Computer Engineering, University of Tabriz, Tabriz, Iran
3,4. Space Trusters Research Institute, Iranian Space Research Center, Tabriz, Iran

ARTICLE INFO

Article History:

Received 05 August 2025
Revised 21 July 2026
Accepted 21 July 2026
Available Online 02 September 2026

Keywords:

Neuro-fuzzy controller
Type-2 neuro-fuzzy control
Hall thruster
Orbital transfer maneuver
Genetic algorithm

ABSTRACT

Orbital transfer utilizing Hall-effect thrusters (HETs) faces significant challenges due to inherent thrust instabilities and nonlinear actuator faults. This study presents a novel application of an optimized Type-2 neuro-fuzzy controller specifically designed to ensure robust maneuvering under severe uncertainty. Unlike prior studies that are primarily restricted to mild fault conditions and limited controller comparisons, the proposed approach is systematically evaluated against a type-1 neuro-fuzzy controller and a conventional linear quadratic regulator. A neural network initializes the control structure, while a genetic algorithm is used solely for fuzzy rule reduction and acceleration of the training process, thereby improving computational efficiency without direct controller tuning. Numerical simulations demonstrate that, under sustained high-amplitude and high-frequency fault scenarios, the proposed Type-2 controller preserves accurate orbital tracking and system stability. In contrast, the comparative methods exhibit significant performance degradation. These results establish a reliable and fault-tolerant control framework for low-Earth orbit missions in which conventional robust control strategies prove inadequate.

*Corresponding Author's E-mail: ghaemi@tabrizu.ac.ir

How to Cite this Article:
M. Mansoury, S. Ghaemi, S. Mir Mazhari Anvar, and M. Farhid, "Optimized Type 2 neuro-fuzzy control for robust orbital maneuvers under hall-effect thruster faults and uncertainty," *Journal of Space Science and Technology*, Vol. VV, No. V, pp. 1-17, 2026, https://doi.org/10.22034/jsst.2026.1561.

1. ABBREVIATIONS AND NOMENCLATURE

Abbreviation/Symbol	Description
Abbreviations	
T2NFC	Type-2 Neuro-Fuzzy Control
HET	Hall-Effect Thruster
ODT2FLC	Optimized Discrete Type-2 Fuzzy Logic Controller
RMSE	Root Mean Square Error
LEO	Low Earth Orbit
J2	Earth's Oblateness Perturbation (J2 effect)
Nomenclature	
a	Semi-major axis of the orbit
e	Eccentricity of the orbit
i	Inclination of the orbit
Ω	Right Ascension of the Ascending Node (RAAN)
ω	Argument of perigee
θ	True anomaly
u	Control input vector
d	Disturbance/Uncertainty vector
ΔV	Velocity change (Delta-V)
η	Efficiency of the actuator

2. INTRODUCTION

Active satellites operating in low Earth orbit (LEO) play a crucial role in modern space missions, serving as key platforms for communication, environmental monitoring, and remote sensing applications [1, 2]. Mission success critically depends on accurate satellite positioning and precise orbital transfer maneuvers, which require advanced control strategies capable of operating under the dynamic, complex conditions of LEO. Various environmental perturbations, including atmospheric drag, solar radiation pressure, and irregular gravitational fields, significantly influence satellite orbital dynamics [3]. These disturbances pose serious challenges to the accurate execution of orbital maneuvers and degrade overall mission performance [4]. Recent studies have addressed these challenges through advanced control strategies designed explicitly for orbital maintenance and transfer using Hall-effect thrusters [5, 6]. Furthermore, the simultaneous requirements of fuel efficiency and long-term system stability further complicate the design of effective orbital control systems. Consequently, the development of robust and intelligent control methodologies has become an essential research objective [5, 6].

Electric propulsion systems, particularly Hall-effect thrusters (HETs), have emerged as practical solutions for LEO missions due to their high efficiency and reduced propellant consumption [7]. Despite these advantages, Hall-effect thrusters are subject to several operational challenges, including dynamic instabilities and stochastic thrust fluctuations. Such imperfections can adversely affect thrust generation accuracy, thereby degrading maneuver precision and compromising orbital control performance [8]. Under these conditions, conventional control schemes often prove insufficient, as they are typically not designed to handle the pronounced nonlinearities and uncertainties inherent to HET-based systems [9].

Model predictive control and optimal control approaches have been widely investigated for satellite orbital maneuvering and maintenance, particularly in low Earth orbit missions employing continuous low-thrust propulsion systems such as Hall-effect thrusters [10–12]. However, their practical effectiveness is often limited by complex structural designs and high computational requirements, particularly in nonlinear and uncertain environments [13]. Alternatively, Lyapunov-based stability analysis methods have been employed to guarantee system stability. Nevertheless, such techniques typically focus on stability assurance and do not simultaneously address fuel optimization or fault tolerance, which are critical requirements for modern space missions.

Among recent studies, linear and nonlinear feedback control strategies have also been developed based on simplified orbital dynamics models; however, their performance deteriorates noticeably in the presence of nonlinear low-thrust dynamics and propulsion uncertainties inherent to Hall-effect thrusters [14]. Although these methods demonstrate satisfactory performance under ideal operating conditions, their effectiveness is significantly reduced when system nonlinearities and actuator faults are present. This limitation is particularly evident in satellites equipped with Hall-effect thrusters, where nonlinear behavior and thrust uncertainties are unavoidable. Consequently, existing studies highlight the absence of a comprehensive control framework capable of simultaneously handling thruster faults, optimizing energy consumption, and maintaining precise orbital trajectory control. These challenges underscore the necessity of advanced control systems that can effectively manage the dynamic and uncertain conditions of Low Earth Orbit while ensuring robust performance [15].

Type-1 neuro-fuzzy controllers, which combine the learning capability of neural networks with the reasoning structure of fuzzy logic, have attracted considerable attention in a wide range of industrial and aerospace applications [16, 17]. By integrating empirical fuzzy rules with adaptive neural learning, these controllers can achieve acceptable performance in nonlinear systems subject to moderate uncertainties. Given the frequent exposure of orbital systems to dynamic variations, external disturbances, and actuator faults, neuro-fuzzy control schemes offer notable advantages in robust control design [18]. However, Type-1 neuro-fuzzy controllers suffer from inherent limitations when applied to highly complex and uncertain environments. These deficiencies mainly arise from fixed membership functions, reliance on predefined fuzzy rules, and dependence on the initial controller structure, which restrict adaptability to unforeseen operating conditions [19]. Moreover, Type-1 fuzzy controllers generally exhibit reduced performance in the presence of severe uncertainties and actuator faults [20, 21], a drawback that is particularly pronounced in Hall-effect thrusters due to their nonlinear and unstable characteristics [22]. More recently, a neuro-fuzzy proportional–derivative attitude controller trained via an adaptive network-based inference scheme has been reported for CubeSat missions subject to combined low-Earth-orbit disturbances, further confirming the growing relevance of neuro-fuzzy architectures for satellite control applications [29].

In this study, an optimized Type-2 neuro-fuzzy control framework is explicitly proposed for satellite orbital transfer maneuvers in Low Earth Orbit, targeting the critical vulnerability of fault-prone Hall-effect thrusters. Although electric propulsion systems offer superior efficiency, they are inherently affected by plasma instabilities and thrust fluctuations, which significantly degrade maneuver accuracy under uncertainty. Unlike existing studies that primarily rely on Type-1 neuro-fuzzy controllers or conventional robust control strategies such as LQR (both of which are generally validated under mild or short-term fault conditions) the present research introduces a systematic application of Type-2 fuzzy logic to address severe, high-frequency, and long-duration actuator faults in orbital transfer missions.

The primary innovation of this work lies not only in employing a Type-2 neuro-fuzzy structure, but in its targeted design for absolute robustness and quantitative comparison under worst-case fault scenarios. The controller is initialized through neural network training using fault-free data. At the same time, a genetic algorithm is employed exclusively for fuzzy rule reduction and training acceleration under noisy conditions, rather than direct controller tuning. This constrained yet effective use of GA distinguishes the proposed framework from conventional neuro-fuzzy-GA approaches by ensuring fast convergence and computational efficiency suitable for time-critical space operations.

Furthermore, a comprehensive comparative analysis with a Type-1 neuro-fuzzy controller and an LQR scheme demonstrates that, while all methods exhibit comparable performance under limited fault exposure, the Type-1 and LQR controllers experience substantial performance degradation when faults persist throughout the mission duration. In contrast, the proposed Type-2 neuro-fuzzy controller preserves stable and accurate trajectory tracking even under intensified fault conditions (amplitude 0.01 and frequency 0.1), thereby validating its superior robustness and effectiveness for fault-tolerant orbital control in uncertain LEO environments.

The remainder of this paper is organized as follows. Section II presents the dynamic modeling of a satellite equipped with a Hall-effect thruster and examines the effects of common actuator faults on system behavior. Section III describes the design of the proposed Type-2 neuro-fuzzy controller, including the genetic algorithm-based optimization of control rules. In Section IV, the effectiveness of the proposed approach is evaluated through numerical simulations, with a detailed analysis of tracking accuracy, stability, and fuel consumption during orbital transfer maneuvers.

3. SATELLITE DYNAMICS AND HALL-EFFECT THRUSTER UNDER FAULT AND DISTURBANCE

This section presents the mathematical modeling of a satellite operating in Low Earth Orbit, along with the dynamic behavior of the Hall-effect thruster as the propulsion actuator. The model includes both the satellite's orbital motion and the thrust-generation mechanism, accounting for actuator faults. The primary objective of this section is to establish a rigorous mathematical foundation for the design of a fault-tolerant control system in the subsequent sections. To this end, environmental disturbances and thruster-induced faults are explicitly incorporated into the system dynamics.

3.1. Satellite Orbital Dynamics

The orbital motion of a satellite in Low Earth Orbit is affected by several environmental and gravitational factors, including Earth's central gravitational attraction, atmospheric drag, solar radiation pressure, and gravitational anomalies. In the Earth-centered inertial reference frame, the satellite's equation of motion can be expressed in vector form as [25]:

$$\frac{d\mathbf{v}}{dt} = -\mu \frac{\mathbf{r}}{|\mathbf{r}|^3} + \mathbf{a}_c + \mathbf{a}_d \tag{1}$$

Where $(\mathbf{v})$ is the velocity of the satellite, $(\mathbf{r})$ represents the position vector of the satellite concerning the Earth's center, (μ) denotes Earth's gravitational parameter, $(\mathbf{a}_c)$ is the acceleration generated by the satellite's control system (provided by the Hall-effect thruster), and $(\mathbf{a}_d)$ is the acceleration due to external disturbances. Equation (1) describes the satellite motion in accordance with Newton's second law, in which Earth's gravity acts as the dominant central force and environmental perturbations are superimposed on the orbital dynamics.

To avoid orbital singularities at particular angles (such as 0 or 180 degrees inclination), a set of modified orbital parameters is employed, which provide a more accurate description of the satellite's orbital characteristics. These parameters, applicable for a range of orbital types from circular to hyperbolic, are defined as (2):

$$\begin{aligned}
z_1 &= \Omega + \omega + \psi, \\
z_2 &= \sqrt{\frac{\mu}{a^3}}, \\
z_3 &= e\cos(\Omega + \omega), \\
z_4 &= e\sin(\Omega + \omega), \\
z_5 &= \tan\left(\frac{i}{2}\right)\cos(\Omega), \\
z_6 &= \tan\left(\frac{i}{2}\right)\sin(\Omega).
\end{aligned} \tag{2}$$

These variables not only provide an accurate depiction of orbital motion but also eliminate singularities under specific geometric conditions, thereby facilitating subsequent analytical and control design procedures. The orbital tracking error is defined as the deviation of the modified orbital elements from their desired reference values. Accordingly, the error vector can be expressed as (3) [26].

$$\begin{aligned}
&\delta_1 = z_1 - z_1^*, \\
&\delta_2 = z_2 / z_2^* - 1, \\
&\begin{bmatrix} \delta_3 \\ \delta_4 \end{bmatrix} = \begin{bmatrix} \cos(z_1) & \sin(z_1) \\ \sin(z_1) & -\cos(z_1) \end{bmatrix} \begin{bmatrix} z_3 - z_3^* \\ z_4 - z_4^* \end{bmatrix}, \\
&\begin{bmatrix} \delta_5 \\ \delta_6 \end{bmatrix} = \begin{bmatrix} \cos(z_1) & \sin(z_1) \\ \sin(z_1) & -\cos(z_1) \end{bmatrix} \begin{bmatrix} z_5 - z_5^* \\ z_6 - z_6^* \end{bmatrix}.
\end{aligned} \tag{3}$$

The error dynamics of the orbital system, considering external disturbances and the thrust force produced by the Hall-effect thruster, are described in (4).

$$\frac{d\delta}{dt} = \mathbf{A}\delta + \mathbf{B}\mathbf{u} + \boldsymbol{\eta}_d \tag{4}$$

Where $(\mathbf{A})$ is the matrix corresponding to the dynamic behavior of the system, and $(\mathbf{B})$ is the matrix representing the effect of the thruster control force on the system (as calculated in [26]). Moreover, $(\boldsymbol{\eta}_d)$ denotes environmental disturbances, which include the effects of atmospheric drag, solar radiation pressure, and gravitational anomalies. The orbital state is propagated directly in terms of the mean orbital elements defined in (2)-(3), using the Gauss variational formulation of [25, 26]; the resulting linear time-varying model is integrated numerically with a fixed discretization step of Δt = 1 s (Appendix, Eq. B), which also defines the temporal resolution of the disturbance and fault models.

3.2. Hall-Effect Thruster Dynamics with Fault

Hall-effect thrusters are widely recognized as advanced electric propulsion devices that employ electric and magnetic fields to accelerate ions and generate thrust. In satellites operating in Low Earth Orbit, the thrust generated by the Hall-effect thruster constitutes the primary source of control acceleration. Accordingly, the control acceleration applied to the satellite dynamics can be expressed as (5). Consistent with the reviewer's observation, only the resultant (net) thrust vector produced by the Hall-effect thruster subsystem is modeled in this study, rather than the number, layout, or individual firing pattern of physical thruster units; this lumped-thrust representation is a common simplification in orbit-level control studies (e.g., [26, 27]) and is adequate for the orbital-transfer time-scale considered.

$$\mathbf{a}_c = \frac{\mathbf{F}_c}{m} \tag{5}$$

Where $(\mathbf{F}_c)$ is the force generated by the Hall-effect thruster and (m) is the total mass of the satellite. The thrust produced by the Hall-effect thruster, considering alignment errors and random noise, is modeled as (6) [27]:

$$\mathbf{F}_c = \mathbf{Q}(\mathbf{q}_{IB}^*)\left[\mathbf{I}_{3\times3} - (\mathbf{R}_T\times)\right]\begin{bmatrix}(1+\kappa_x)F_{cX} + \nu_x \\ (1+\kappa_y)F_{cY} + \nu_y \\ (1+\kappa_z)F_{cZ} + \nu_z\end{bmatrix} \tag{6}$$

Where $(\mathbf{Q}(\mathbf{q}_{\mathrm{IB}}^*))$ is the transformation matrix from the body frame to the inertial frame, $\mathbf{R}_T$ is the thruster misalignment error, (κ_i) is the misalignment error coefficients, and (ν_i) is the random noise in the (x, y, z) axes. The random noise is described by model (7):

$$E[\nu_i(t)\nu_i(t')^T] = \sigma_i^2\delta(t-t') \tag{7}$$

Where (σ_i^2) is the noise variance and $(\delta(t-t'))$ is the impulse function. This model accurately reflects the effects of thruster faults on the generation of control force. In terms of statistical characterization, the random component in Eq. (7) is modeled as a zero-mean, bounded stochastic process, while the deterministic fault term in Eq. (9) is bounded by the sinusoidal amplitude-frequency pairs examined in the simulation section, namely (0.001, 0.05) for the limited-fault case and (0.01, 0.1) for the severe-fault case; these two pairs define the lower and upper uncertainty bounds evaluated throughout this study.

To further evaluate the thruster performance under fault and degradation conditions, additional structural errors are introduced into the thrust model. Accordingly, the modified thruster output used in the simulation studies is given by (8):

$$\mathbf{F}_c = \mathbf{M}(\mathbf{I}_{3\times3} - \boldsymbol{\delta}_p)\begin{bmatrix}(1+\lambda_p)u_c \\ 0 \\ 0\end{bmatrix} + \mathbf{n}(t) \tag{8}$$

Where $(\mathbf{M})$ is the transformation matrix, $(\boldsymbol{\delta}_p)$ is the misalignment error coefficients resulting from the satellite body state and system structure, (λ_p) is the thruster functional error parameter, (u_c) is the control signal, and $(\mathbf{n}(t))$ is the occurred fault, which can be considered as in equation (9).

$$\mathbf{n}(t) = \begin{bmatrix}0.001\sin(0.05t) \\ 0.001\sin(0.05t) \\ 0.001\sin(0.05t)\end{bmatrix}. \tag{9}$$

In this model, $\mathbf{n}(t)$ represents the time-varying sinusoidal noise, which affects the thrust force with a small amplitude and limited frequency. These noises are applied as brief instabilities in the thruster force to investigate the effects of thruster faults in the simulation of the orbital transfer process.

3.3. Disturbances Affecting the System

Environmental disturbances acting on satellites play a critical role in the stability and performance of orbital control systems. These disturbances consist of non-conservative forces and external dynamic effects that influence satellite motion through additional acceleration components. To accurately model their impact, the acceleration associated with each disturbance source is computed individually, and the total disturbance acceleration is obtained by superposition.

In Low Earth Orbit, atmospheric drag represents the dominant non-gravitational force acting on a satellite. This force arises from collisions with atmospheric particles and depends on the satellite's relative velocity and local atmospheric density. The resulting acceleration due to atmospheric drag is expressed as (10):

$$\vec{a}_{\mathrm{drag}} = \frac{1}{2}\rho v_{\mathrm{rel}}^2 \cdot \frac{SC_D}{m} \tag{10}$$

Where m is the satellite mass, S is the effective cross-sectional area of the satellite, C_D is the drag coefficient, ρ is the atmospheric density, and v_{rel} is the relative velocity of the satellite concerning the atmosphere. Another significant disturbance is due to the Earth's gravity. Due to the non-spherical shape of the Earth and its uneven mass distribution, specific gravitational effects act on the satellite, which are often analyzed in terms of the J2 component (Earth's oblateness coefficient). The acceleration resulting from this deviation from sphericity is expressed as (11):

$$\vec{a}_{J_2} = \frac{3J_2\mu R^2}{2r^5}\left[\left(5\frac{(\vec{r}\cdot\bar{K}_E)^2}{r^2}-1\right)\vec{r}-2(\vec{r}\cdot\bar{K}_E)\bar{K}_E\right] \quad (11)$$

Where R is the Earth's radius, μ is the Earth's gravitational constant, r is the distance from the satellite to the Earth's center, $\vec{r}$ is the position vector of the satellite, and $\bar{K}_E$ is the direction of the Earth's polar axis. Solar radiation is another source of disturbance, applying radiation pressure force on the satellite's surface. This force depends on the distance from the satellite to the Sun and the characteristics of the satellite's surface. The acceleration due to radiation pressure is modeled as (12):

$$\vec{a}_{srb} = -PC_R\frac{A}{m}\frac{\vec{r}_{\text{sat-sun}}}{\|\vec{r}_{\text{sat-sun}}\|^3}AU^2 \quad (12)$$

Where P is the mean solar radiation momentum flux, C_R is the reflectivity coefficient, A is the effective area facing the Sun, AU is the astronomical unit, and $\vec{r}_{\text{sat-sun}}$ is the vector from the satellite to the Sun. The gravitational influence of other celestial bodies, such as the Moon and the Sun, is also exerted on the satellite as a third-body force. This acceleration is modeled as (13):

$$\begin{aligned}\vec{a}_{sun} &= \mu_{sun}\left(\frac{\vec{r}_{\text{sun/sc}}}{r^3_{\text{sun/sc}}}-\frac{\vec{r}_{\text{sun/earth}}}{r^3_{\text{sun/earth}}}\right)\\ \vec{a}_{moon} &= \mu_{moon}\left(\frac{\vec{r}_{\text{moon/sc}}}{r^3_{\text{moon/sc}}}-\frac{\vec{r}_{\text{moon/earth}}}{r^3_{\text{moon/earth}}}\right)\end{aligned} \quad (13)$$

Where μ_{sun} and μ_{moon} are the gravitational constants of the Sun and the Moon, respectively, and $\vec{r}_{\text{sun/sc}}$, $\vec{r}_{\text{moon/sc}}$, $\vec{r}_{\text{sun/earth}}$, and $\vec{r}_{\text{moon/earth}}$ are the position vectors between the satellite, the Moon, the Sun, and the Earth, respectively. Finally, the total disturbance acceleration acting on the satellite is summarized in vector form as (14):

$$\gamma_p = \vec{a}_{\text{drag}} + \vec{a}_{J_2} + \vec{a}_{srb} + \vec{a}_{sun} + \vec{a}_{moon} \quad (14)$$

This vector represents the cumulative effect of environmental disturbances and is explicitly incorporated into the control-oriented satellite dynamics.

4. OPTIMIZED TYPE-2 NEURO-FUZZY CONTROLLER DESIGN

In this section, the introduction and development of an advanced control architecture for managing satellite dynamics during orbital transfer operations is presented, with an emphasis on compensating the effects of Hall-effect thruster performance faults. The proposed approach integrates the advantages of Type-2 fuzzy logic and the learning capabilities of neural networks, employing the Mamdani type for generating the control output. Additionally, a genetic algorithm will be utilized to optimize the extracted fuzzy rules. This hybrid methodology ensures high adaptability and robust performance in the face of uncertainties and disturbances. The overall structure of this section includes three main parts: introduction of the Type-2 neuro-fuzzy controller, explanation of the Mamdani structure in this controller, and clarification of the fuzzy rule optimization process using a genetic algorithm.

4.1. Mamdani Type-2 Neuro-Fuzzy Controller

A Type-2 fuzzy set is characterized by a three-dimensional membership function that includes an additional degree of freedom to represent uncertainty explicitly. This uncertainty is quantified through the Footprint of Uncertainty (FOU), which is bounded by an upper and a lower Type-1 membership function. The presence of the FOU enables Type-2 Fuzzy Logic Controllers (T2FLCs) to handle greater levels of uncertainty than conventional Type-1 fuzzy systems.

In this study, a Mamdani-type Type-2 neuro-fuzzy controller is employed. While the controller follows the classical if–then fuzzy rule structure, the utilization of Type-2 fuzzy sets in the rule consequents significantly improves robustness against uncertainties. Unlike Type-1 controllers, which rely on crisp membership values, Type-2 fuzzy systems exploit the FOU to model system nonlinearities, parameter variations, and unmodeled dynamics more effectively.

The architecture of the proposed Mamdani Type-2 neuro-fuzzy controller consists of multiple interconnected layers that execute the control process sequentially. In the fuzzification layer, the system inputs (namely the tracking error δ and its time derivative $\dot{\delta}$) are mapped onto Type-2 fuzzy sets. The corresponding membership functions are defined over the FOU to capture uncertainty in the input space and are mathematically expressed as (15):

$$\tilde{\mu}_A(\delta) = \{(\mu_A^L(\delta), \mu_A^U(\delta)) \mid \delta \in D\} \tag{15}$$

Where $\mu_A^L(\delta)$ and $\mu_A^U(\delta)$ are, respectively, the lower and upper bounds of the input membership function A, and D is the definition domain of the input data. After fuzzification, the Type-2 fuzzy rules are implemented as a set of if-then conditional statements. Each rule is represented as (16):

$$R_i : \text{IF } \delta \text{ is } \tilde{A}_i \text{ AND } \dot{\delta} \text{ is } \tilde{B}_i \text{ THEN } u \text{ is } \tilde{C}_i \tag{16}$$

Where $\tilde{A}$, $\tilde{B}$, and $\tilde{C}$ are, respectively, the Type-2 fuzzy sets corresponding to the input and output variables. Utilizing these rules, the fuzzy inference engine analyzes the fuzzified input values and calculates the firing strength (degree of activation) of each rule. Unlike Type-1 fuzzy systems, which generate the rule outputs as a single numerical value, the output of Type-2 systems is a Type-1 fuzzy set. This output requires a type-reduction step to convert it into an interval. One of the widely used methods for this purpose is the centroid (center of sets) method, which determines the output value as (17):

$$u = \frac{\int_{\text{FOU}} \xi \cdot \mu_{\tilde{C}}(\xi) d\xi}{\int_{\text{FOU}} \mu_{\tilde{C}}(\xi) d\xi} \tag{17}$$

Where ξ is the fuzzy output member and $\mu_{\tilde{C}}(\xi)$ is the type-reduced membership function. After type reduction, the defuzzification stage generates a single crisp control signal u, which is applied to the Hall-effect thruster. To further enhance adaptability and performance, a neural network is incorporated to automatically adjust the parameters of the membership functions and fuzzy rules. The neural network employs an adaptive learning mechanism driven by system inputs to minimize the control error. This integration enables the proposed controller to effectively cope with nonlinear behavior, time-varying dynamics, and high levels of uncertainty, thereby ensuring accurate and stable orbital control performance.

4.2. Optimization of Fuzzy Rules Using Genetic Algorithm

To achieve optimal performance of the Mamdani Type-2 neuro-fuzzy controller, a genetic algorithm (GA) is employed to optimize the fuzzy rule base. One of the principal challenges in designing neuro-fuzzy controllers lies in selecting an appropriate set of if–then rules with proper structure and cardinality. As the number of inputs and membership functions increases, the rule base grows exponentially, making manual tuning highly impractical and prone to suboptimal solutions.

In the proposed approach, each fuzzy rule set is encoded into a chromosome within the GA search space. Each chromosome represents a complete combination of fuzzy rules defined in (16) and is modeled as a numerical vector whose elements correspond to the selected fuzzy sets. To evaluate the effectiveness of each chromosome, a fitness function F is defined to quantify control performance. This function typically balances tracking accuracy and energy consumption and is expressed as (18):

$$F = \frac{1}{\alpha \cdot ISE + \beta \cdot E} \tag{18}$$

Where α and β are weights for tuning the importance of control accuracy (ISE) and energy consumption (E), respectively. Lower values of ISE indicate more minor deviations of the system from ideal performance, while E represents the energy consumed by the thrusters.

The genetic algorithm begins with the initial generation of a random population of chromosomes. In each generation, natural selection is applied to identify the more promising chromosomes. Chromosomes are ranked according to the value of the fitness function [F], and the better-performing chromosomes are selected for generating new chromosomes through crossover and mutation operators. The crossover operator involves exchanging segments of information between two parent chromosomes to produce offspring chromosomes. At the same time, mutation introduces random changes in specific segments of the chromosomes to increase diversity and avoid being trapped in local minima. In this process, the new chromosome R_{new} is defined as a combination of the rules of the two parent chromosomes R_1 and R_2, as formulated in (19):

$$R_{\text{new}} = \lambda R_1 + (1-\lambda) R_2 \tag{19}$$

Where λ is a random weighting parameter selected between 0 and 1, additionally, random mutation with probability P_{mut} is applied to some of the genes in the chromosome, as represented in (20):

$$R_{\text{mutated}}(i) = R_{\text{original}}(i) + \epsilon \tag{20}$$

In this context, ϵ is a small random value introduced to induce local changes in the rules. This process is repeated generation by generation until the algorithm reaches the convergence criterion, i.e., when the change in the mean fitness value of the population falls below a predefined threshold. Ultimately, the chromosome with the highest value of F among the population is chosen as the optimal set of fuzzy rules.

The application of the genetic algorithm for optimal rule design enables a reduction in the complexity of manual design. It increases the accuracy of the search within the rule space, thereby optimizing the performance of the Mamdani Type-2 neuro-fuzzy controller under complex orbital conditions and in the presence of environmental disturbances and thruster faults. This approach, in addition to ensuring system stability, significantly reduces its sensitivity to uncertainties.

5. SIMULATION AND RESULTS

In this section, the performance of the proposed optimized Type-2 neuro-fuzzy controller is evaluated through comprehensive simulation studies carried out under Hall-effect thruster fault conditions. The objective is to investigate the robustness and fault-tolerant capability of the controller during low-thrust orbital transfer maneuvers.

All orbital parameters, environmental constants, thruster characteristics, and controller configuration values employed in the simulations are summarized in Table 1.

Initially, the training dataset required for constructing the Type-2 neuro-fuzzy controller was generated using an LQR-based orbital control strategy [28], applied to the linearized satellite dynamics. The acquired state–control pairs provided a reference dataset that covers the entire orbital transfer window and serves as a benchmark for learning the control policy.

A Type-2 neuro-fuzzy structure was then constructed, combining a neural network learning stage with a Takagi–Sugeno fuzzy inference mechanism. After the training phase, the controller automatically extracted an initial fuzzy rule base from the dataset. To limit computational complexity and ensure fast convergence, the training process was intentionally restricted to a small number of learning epochs. The resulting fuzzy structure forms the basis for subsequent optimization and performance evaluation. In the current simulation study, the collected dataset consisted of 86,401 samples across 6 variables, represented as a double-precision matrix of size 86,401-by-6. To ensure a robust evaluation, this data was partitioned into a training set comprising 80 percent of the total samples and a testing set containing the remaining 20 percent. The ANFIS structure was generated using the Grid Partition method, in which 3 membership functions were assigned to each input variable, so that the initial fuzzy rule base could systematically cover the input space. The neuro-fuzzy controller architecture was then trained for 10 epochs. Furthermore, the genetic algorithm was configured with a population size of 20, a crossover fraction of 0.8, a mutation rate of 0.01, an elitism count of 2, and a maximum of 50 generations to optimize the system parameters. To ensure a realistic simulation environment, the satellite's orbital dynamics are propagated in the Earth-Centered Inertial (ECI) frame by incorporating the dominant environmental perturbations, including Earth's J_2oblateness, atmospheric drag, solar radiation pressure (SRP), and the gravitational influence of third bodies (the Sun and the Moon). The total perturbing acceleration is modeled through the superposition of these individual components, where atmospheric drag is calculated based on the spacecraft's effective cross-section and drag coefficient, while gravitational anomalies and SRP are determined using the J_2constant and the solar momentum flux, respectively. These disturbances are mathematically formulated and integrated into the propagator to evaluate the controller's robustness under non-ideal orbital conditions. All relevant physical constants and simulation parameters (including the J_2coefficient (1.08263×10^{-3}), the solar radiation flux (4.56×10^{-6} N/m²), the astronomical unit (1.496×10^{8} km), and the third-body gravitational parameters) are summarized in the expanded Table 1 to ensure the transparency and reproducibility of the orbital propagation model.

Table 1. Orbital Parameters, Physical Constants, and Controller Configuration Used in Simulations.

Parameter	Value
Initial semi-major axis	6821 km
Final semi-major axis	7371 km
Initial inclination	82°
Final inclination	81°
Earth gravitational parameter	398600.47 km^3/s^2
Earth radius	6378.1363 km
Drag coefficient	2.5
Number of neurons in neural network	524
Number of initial fuzzy rules	243
Final RMSE after optimization	1.78×10^{-2}
Earth oblateness coefficient (J_2)	1.08263×10^{-3}
Astronomical unit (AU)	1.496×10^{8} km
Solar radiation momentum flux	4.56×10^{-6} N/m^2
Discretization time step (Δt)	1 s

The training dataset required for constructing the Type-2 neuro-fuzzy controller was generated using an LQR-based orbital control strategy applied to the linearized satellite dynamics. The resulting state–control pairs cover the entire transfer interval and serve as a reference dataset for learning the control policy.

A Type-2 neuro-fuzzy structure was then developed by integrating a neural network learning phase with a Takagi–Sugeno fuzzy inference mechanism. Following the training stage, an initial fuzzy rule base was automatically extracted from the dataset. To limit computational burden and ensure rapid convergence, the number of learning epochs was intentionally kept low. This trained structure served as the basis for subsequent optimization and closed-loop simulations.

To enhance controller accuracy and robustness under Hall-effect thruster fault conditions, a genetic algorithm was employed to optimize the extracted fuzzy rules. During this stage, redundant and ineffective rules were removed, while efficient rules were preserved and fine-tuned. The root-mean-square error was adopted as the fitness criterion in the optimization process, thereby improving adaptation capabilities in the presence of actuator faults and uncertainties.

Figure 1 shows the response surface of the optimized Type-2 neuro-fuzzy controller with respect to variations in thruster fault magnitude and uncertainty levels. The smooth, continuous surface indicates consistent controller behavior across a wide operating range, confirming the effectiveness of the Type-2 fuzzy framework in handling uncertainty.

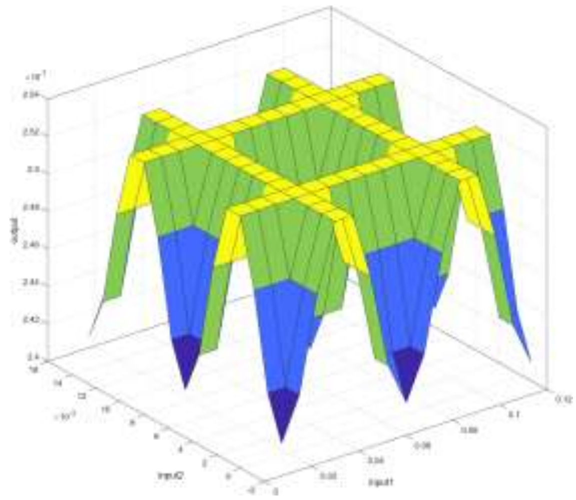

Fig. 1. Response surface of the Type-2 neuro-fuzzy controller to Hall-effect thruster faults and uncertainties.

Figure 2 illustrates the optimized input membership functions of the Type-2 neuro-fuzzy controller obtained after the genetic optimization and rule refinement processes. These membership functions demonstrate enhanced uncertainty representation and reflect the improved adaptability of the controller after optimization. Unlike the simplified Takagi-Sugeno models, this Mamdani-based structure employs a comprehensive rule base consisting of 243 fuzzy if-then rules, mapping five input variables to the control output through linguistic variables and interval-valued fuzzy sets. The inference process utilizes the min-max operator for rule evaluation and Mamdani implication, followed by the Karnik-Mendel algorithm for type-reduction to handle the footprint of uncertainty. Finally, the centroid defuzzification method is applied to transform the aggregated fuzzy output into a crisp control signal, providing a more interpretable and stable command for the satellite's orbital maneuvers. Fig. 3 presents the complete closed-loop block diagram of the proposed Type-2 neuro-fuzzy control system for orbital transfer under Hall-effect thruster fault conditions. This figure highlights the interaction between the satellite dynamical model, the faulty thruster subsystem, and the optimized controller.

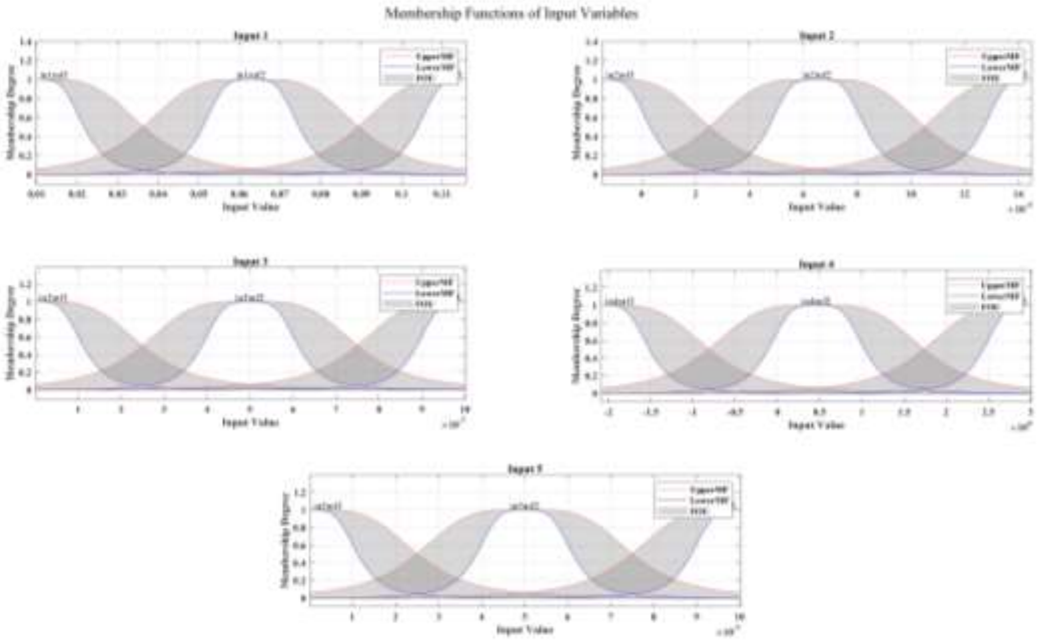

Fig. 2. Input membership functions of the optimized Type-2 neuro-fuzzy controller.

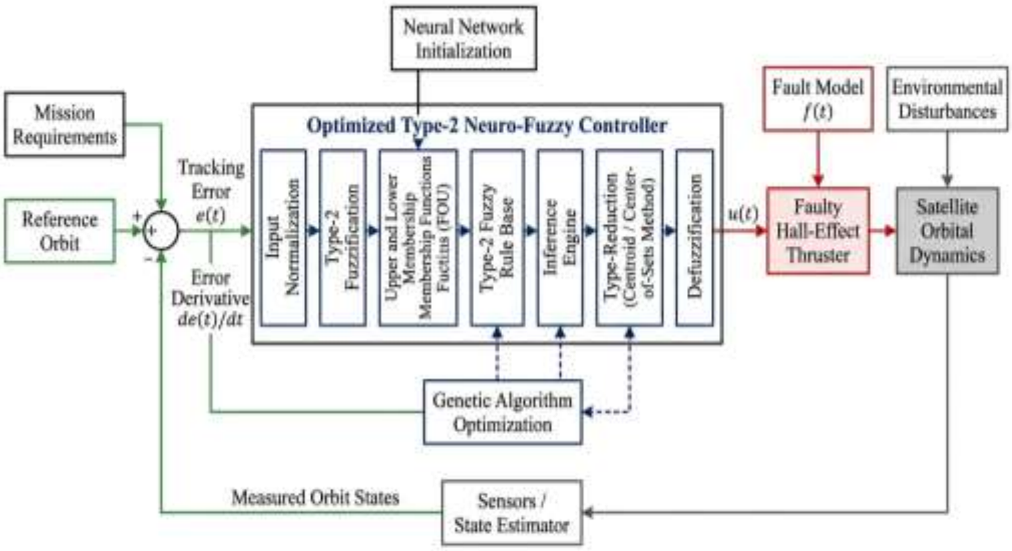

Fig. 3. Block diagram of the optimized Type-2 neuro-fuzzy control system for orbital transfer under Hall-effect thruster faults.

The orbital transfer scenario considered in the simulations involves a transition between two circular orbits with a prescribed change in orbital inclination, while maintaining near-zero eccentricity throughout the maneuver. The remaining orbital elements are left unconstrained due to their negligible influence on the transfer dynamics. All underlying orbital and environmental assumptions are summarized in Table I. Fig. 4 depicts the time-domain evolution of the orbital elements during the transfer maneuver. Despite the presence of sinusoidal disturbances induced by Hall-effect thruster faults, the optimized Type-2 neuro-fuzzy controller successfully drives the semi-major axis, eccentricity, and inclination toward their desired values within the simulation time span.

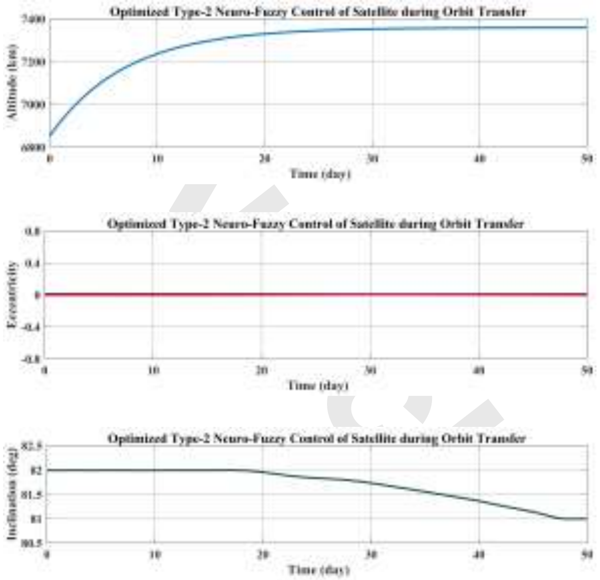

Fig. 4. Performance of the Type-2 neuro-fuzzy controller in correcting the variations of the semi-major axis, eccentricity, and inclination of the satellite under thruster faults.

Figure 5 illustrates the evolution of the control signal generated by the optimized Type-2 neuro-fuzzy controller during the orbital transfer operation. As observed, despite the adverse effects of the Hall-effect thruster fault, the control output gradually converges towards zero, indicating the preservation of system equilibrium and stability throughout the process.

The capability of this controller for dynamic adaptation to changing conditions and handling disturbances is owed to its Type-2 structure and the optimization of fuzzy rules; therefore, even in the presence of severe sinusoidal faults, the system does not experience disarray or performance degradation.

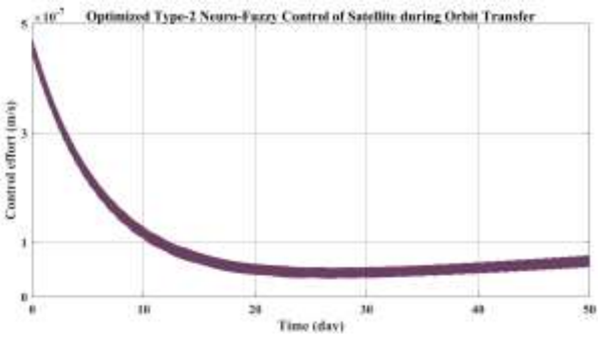

Fig. 5. Control signal generated by the optimized Type-2 neuro-fuzzy controller under Hall-effect thruster fault conditions.

Subsequently, Fig. 6 illustrates the output thrust force of the thruster using a magnified time window corresponding to one representative day of the 50-day mission. This zoomed-in view is deliberately selected to clearly demonstrate the local behavior and variations of the generated thrust. As can be observed, the thrust force closely follows the control signal produced by the optimized Type-2 neuro-fuzzy controller, highlighting the capability of the proposed control scheme to effectively compensate for instabilities and performance degradation induced by thruster faults.

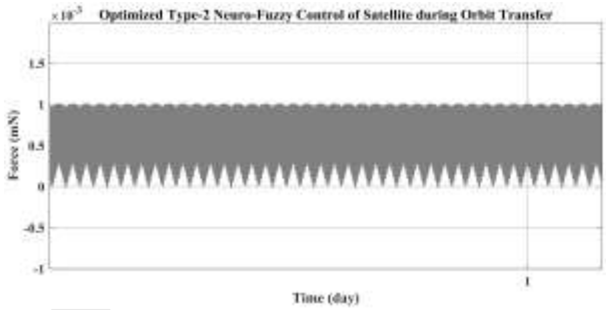

Fig. 6. Thrust force produced by the Hall-effect thruster in the presence of thruster fault.

Next, in order to evaluate the performance of the optimized Type-2 neuro-fuzzy controller under more challenging conditions, the amplitude of the sinusoidal thruster fault, according to Eq. (9), was increased to 0.01 and its frequency to 0.1. These values are noticeably higher than those presented in the baseline scenario of the previous results (where the amplitude was 0.001 and the frequency was 0.05). Increasing the fault intensity implies that the control system is exposed to larger and faster perturbations. Nevertheless, simulation results show that the proposed controller, despite such significant faults, still manages to guide the orbital transfer process with high accuracy and stability. The variations in the semi-major axis, eccentricity, and inclination are entirely kept under control, avoiding any substantial oscillation or severe deviation. This demonstrates the robustness, responsiveness, and high adaptability of the optimized Type-2 structure in the presence of high levels of uncertainty and fault. Figure 7 presents the time responses of the semi-major axis, eccentricity, and inclination of the satellite under these conditions.

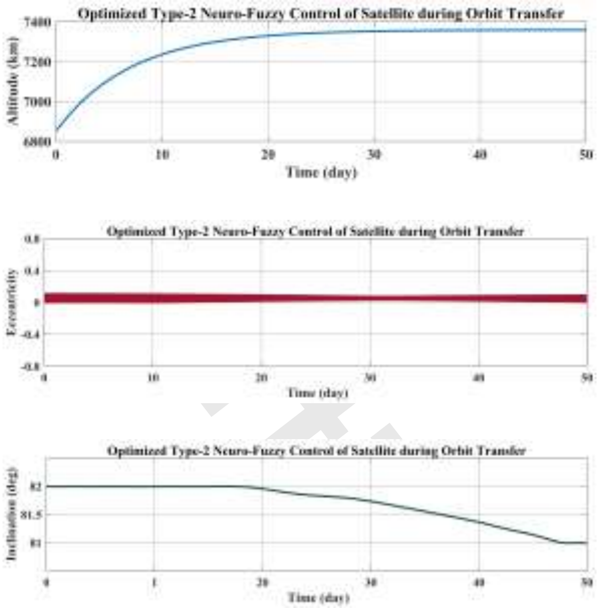

Fig. 7. Time response of orbital parameters (altitude, eccentricity, and inclination) under severe Hall-effect thruster faults and optimized Type-2 neuro-fuzzy control.

To analyze the system's control behavior under these conditions, the output control signal is presented in Fig. 8, confirming the system's convergence and appropriate adaptive response. Furthermore, Fig. 9 shows the thrust force generated by the Hall-effect thruster, with a magnified segment of one operational day to enhance visibility of thrust variations. The strong correspondence and coordination between the generated thrust and the associated control signal clearly demonstrate the efficiency and robustness of the proposed control strategy, particularly in capturing the thruster's dynamic response under faulty operating conditions.

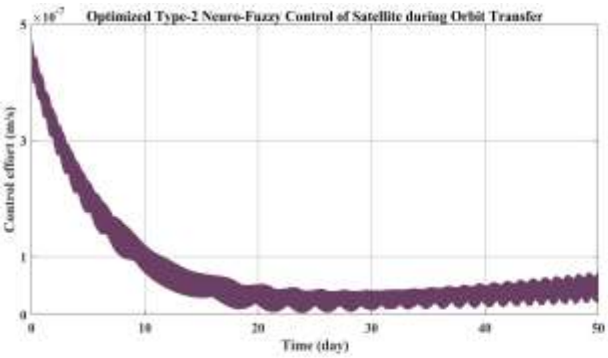

Fig. 8. Control signal generated by the optimized Type-2 neuro-fuzzy controller under high amplitude and frequency thruster fault.

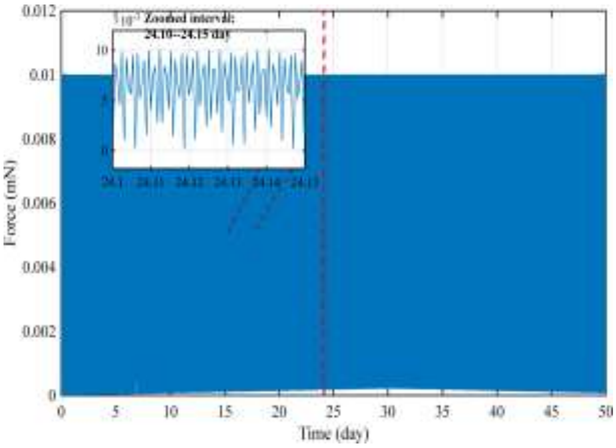

Fig. 9. Variations of the Hall-effect thruster output force under severe fault condition and implementation of the optimized Type-2 neuro-fuzzy controller.

To further quantify the robustness of the proposed control framework and clearly highlight its advantages over existing approaches, a comparative analysis is conducted against a Type-1 neuro-fuzzy controller and a conventional LQR. Two distinct fault scenarios are considered to evaluate controller performance under both limited and persistent fault conditions.

In Scenario 1, actuator faults are applied only during a short interval between days 20 and 25. Under this limited fault exposure, the performance of the Type-2 neuro-fuzzy controller remains comparable to that of the Type-1 neuro-fuzzy approach, while both methods outperform the LQR in terms of orbital accuracy. In Scenario 2, faults are imposed continuously over the entire 50-day transfer period. In this case, the performance of the Type-1 neuro-fuzzy controller and the LQR deteriorates significantly due to their reduced tolerance to sustained uncertainty. In contrast, the proposed Type-2 neuro-fuzzy controller preserves stable tracking and exhibits only marginal performance degradation, demonstrating superior robustness against long-term fault effects.

The quantitative comparison of the RMSE values for the semi-major axis, eccentricity, and inclination under both scenarios is summarized in Table 2.

Table 2. Quantitative performance comparison of Type-2 neuro-fuzzy, Type-1 neuro-fuzzy, and LQR controllers [28] under limited and global fault scenarios.

Parameter [Unit]	Scenario 1: Neuro-Fuzzy T2	Scenario 1: Neuro-Fuzzy T1	Scenario 1: LQR	Scenario 2: Neuro-Fuzzy T2	Scenario 2: Neuro-Fuzzy T1	Scenario 2: LQR
RMSE(a) [km]	1.95×10^{-3}	2.10×10^{-3}	3.07×10^{-3}	2.15×10^{-3}	1.43×10^{-2}	2.68×10^{-2}
RMSE(e) [–]	9.06×10^{-4}	9.82×10^{-4}	1.45×10^{-3}	1.14×10^{-3}	7.97×10^{-3}	1.05×10^{-2}
RMSE(i) [deg]	3.20×10^{-4}	3.51×10^{-4}	5.34×10^{-4}	3.88×10^{-4}	4.67×10^{-4}	7.33×10^{-4}

6. CONCLUSION

This study presented an optimized Type-2 neuro-fuzzy control framework for robust orbital transfer maneuvers of satellites equipped with Hall-effect thrusters operating under severe and persistent fault conditions. In contrast to earlier studies that predominantly address mild disturbances, short-duration uncertainties, or conventional neuro-fuzzy structures, the proposed controller was explicitly designed, trained, and evaluated under high-amplitude and high-frequency thruster faults, representing a more realistic and challenging operational environment. Simulation results confirm that the controller maintains stable, accurate orbital tracking while effectively regulating key orbital parameters (including the semi-major axis, eccentricity, and inclination) even when actuator faults remain active throughout the mission. The smooth convergence of the control signal and the consistent thrust coordination further validate the robustness and practical feasibility of the proposed architecture for long-term orbital maneuvering. A central contribution of this study lies in the purposefully constrained use of the genetic algorithm, which was employed exclusively for fuzzy-rule reduction and training-time acceleration rather than for direct controller tuning. This ensures computational efficiency and rapid convergence during training without introducing unnecessary optimization complexity.

Moreover, the comparative analysis in Section 4 demonstrates that although Type-1 neuro-fuzzy and LQR controllers perform adequately at low disturbance levels, both methods exhibit significant degradation at fault amplitudes of 0.01 and fault frequencies of 0.1. In contrast, the proposed Type-2 controller preserves precise trajectory tracking and robust performance under the same challenging conditions. These comparative results quantitatively validate the superiority and operational reliability of the optimized Type-2 neuro-fuzzy framework.

Overall, the findings confirm that the proposed controller offers a reliable, fault-tolerant, and computationally efficient solution for Hall-effect-based orbital maneuvering, extending the applicability of intelligent control methods to highly uncertain and fault-prone space environments.

7. ACKNOWLEDGEMENT

The authors would like to sincerely thank the Iranian Space Research Institute for its financial support and provision of a suitable platform, which enabled the execution of this research. The scientific cooperation and support of the University of Tabriz and the Space Propulsion Research Institute have also had a significant impact on achieving the objectives of this study. Special thanks are extended to all colleagues, advisors, and friends whose guidance and participation contributed to the advancement of this project.

CONFLICT OF INTEREST

The authors declare that they have no conflict of interest.

REFERENCES

[1] J. A. Starek, B. Açıkmeşe, I. A. Nesnas, and M. Pavone, "Spacecraft autonomy challenges for next-

generation space missions," in *Advances in Control System Technology for Aerospace Applications*, E. Feron, Ed. Heidelberg, Berlin, Springer, 2015, pp. 1-48. https://doi.org/10.1007/978-3-662-47694-9_1.

[2] N. Li, H. Sun, and Q. Zhang, "Robust passive adaptive fault tolerant control for stochastic wing flutter via delay control," *European Journal of Control*, vol. 48, pp. 74-82, 2019, https://doi.org/10.1016/j.ejcon.2019.04.008.

[3] A. A. Amin and K. Mahmood-ul-Hasan, "Robust passive fault tolerant control for air fuel ratio control of internal combustion gasoline engine for sensor and actuator faults," *IETE Journal of Research*, vol. 69, no. 5, pp. 2846-2861, 2023, https://doi.org/10.1080/03772063.2021.1906767.

[4] M. Leomanni, A. Garulli, A. Giannitrapani, and F. Scortecci, "Propulsion options for very low Earth orbit microsatellites," *Acta Astronautica*, vol. 133, pp. 444-454, 2017, https://doi.org/10.1016/j.actaastro.2016.11.001.

[5] S. Ueda and A. Noumi, "Precise rendezvous guidance in low earth orbit via machine learning," in *International Symposium on Control Systems (SICE ISCS)*, Kumamoto, Japan, 2019, pp. 27-32, https://doi.org/10.23919/SICEISCS.2019.8758738.

[6] M. Saied, B. Lussier, I. Fantoni, H. Shraim, and C. Francis, "Active versus passive fault-tolerant control of a redundant multirotor UAV," *The Aeronautical Journal*, vol. 124, no. 1273, pp. 385-408, 2020, https://doi.org/10.1017/aer.2019.149.

[7] D. O'Reilly, G. Herdrich, and D. F. Kavanagh, "Electric propulsion methods for small satellites: A review," *Aerospace*, vol. 8, no. 1, 2021, Art. no. 22, https://doi.org/10.3390/aerospace8010022.

[8] J. D. Stefanovski, "Passive fault tolerant perfect tracking with additive faults," *Automatica*, vol. 87, pp. 432-436, 2018, https://doi.org/10.1016/j.automatica.2017.09.011.

[9] M. Pontani and M. Pustorino, "Nonlinear Earth orbit control using low-thrust propulsion," *Acta Astronautica*, vol. 179, pp. 296-310, 2021, https://doi.org/10.1016/j.actaastro.2020.10.037.

[10] M. Kiantaj, M. Farhid, and M. Shameli, "Robust model predictive control for satellite orbit maintenance using hall effect thrusters," *Journal of Technology in Aerospace Engineering*, vol. 8, no. 4, pp. 27-38, 2024, (in Persian), https://doi.org/10.22034/jtae.2024.8.4.3.

[11] M. Pontani and M. Pustorino, "Nonlinear Earth orbit control using low-thrust propulsion," *Acta Astronautica*, vol. 179, pp. 296-310, 2021, https://doi.org/10.1016/j.actaastro.2020.10.037.

[12] M. Mansoury, M. A. Badamchizadeh, and H. Kharrati, "Stochastic Model Predictive Control Based on Online Learning for a Class of Nonlinear Constrained Systems," in *32nd International Conference on Electrical Engineering (ICEE)*, Tehran, Iran, 2024, pp. 1-7, https://doi.org/10.1109/ICEE63041.2024.10667954.

[13] Y. Gui, Q. Jia, H. Li, and Y. Cheng, "Reconfigurable fault-tolerant control for spacecraft formation flying based on iterative learning algorithms," *Applied Sciences*, vol. 12, no. 5, 2022, Art. no. 2485, https://doi.org/10.3390/app12052485.

[14] Y. Mu, H. Zhang, R. Xi, Z. Wang, and J. Sun, "Fault-tolerant control of nonlinear systems with actuator and sensor faults based on T–S fuzzy model and fuzzy observer," *IEEE Transactions on Systems, Man, and Cybernetics: Systems*, vol. 52, no. 9, pp. 5795-5804, 2021, https://doi.org/10.1109/TSMC.2021.3131495.

[15] D. Izzo, M. Märtens, and B. Pan, "A survey on artificial intelligence trends in spacecraft guidance dynamics and control," *Astrodynamics*, vol. 3, no. 4, pp. 287-299, 2019, https://doi.org/10.1007/s42064-018-0053-6.

[16] J. P. Zand, J. Katebi, and S. Yaghmaei-Sabegh, "A hybrid clustering-based type-2 adaptive neuro-fuzzy forecasting model for smart control systems," *Expert Systems with Applications*, vol. 239, 2024, Art. no. 122445, https://doi.org/10.1016/j.eswa.2023.122445.

[17] S. Danyali, M. Babaeifard, M. Shirkhani, A. Azizi, J. Tavoosi, and Z. Dadvand, "A new neuro-fuzzy controller based maximum power point tracking for a partially shaded grid-connected photovoltaic system," *Heliyon*, vol. 10, no. 17, 2024, Art. no. e36747, https://doi.org/10.1016/j.heliyon.2024.e36747.

[18] A. Safari and S. Ghaemi, "NeuroFuzzyMan: A hybrid neuro-fuzzy BiLSTM stacked ensemble model for financial forecasting and analysis: Dataset case studies on JPMorgan, AMZN and TSLA," *Expert Systems with Applications*, vol. 266, 2025, Art. no. 126037, https://doi.org/10.1016/j.eswa.2024.126037.

[19] J. Tavoosi, A. Mohammadzadeh, and K. Jermsittiparsert, "A review on type-2 fuzzy neural networks for system identification," *Soft Computing*, vol. 25, no. 10, pp. 7197-7212, 2021, https://doi.org/10.1007/s00500-021-05686-5.

[20] A. Attar, M. A. Badamchizadeh, and S. Ghaemi, "Designing of type-2 fuzzy formation controller for a class of nonlinear multiagent system using JAYA algorithm," in *32nd International Conference on Electrical Engineering (ICEE)*, Tehran, Iran, 2024, pp. 1-8, https://doi.org/10.1109/ICEE63041.2024.10667744.

[21] A. Aran, M. Mansoury, S. Ghaemi, and J. Katebi, "Designing a fuzzy-based hybrid control system to reduce structure vibration using rooftop tank and MR damper," *Journal of Civil and*

Environmental Engineering, vol. 55, no. 1, pp. 69-83, 2025, (in Persian), https://doi.org/10.22034/CEEJ.2025.62705.2374.

[22] M. Kiantaj, M. Farhid, and M. Shameli, "Robust model predictive control for satellite orbit maintenance using hall effect thrusters," *Journal of Technology in Aerospace Engineering*, vol. 8, no. 4, pp. 27-38, 2024, (in Persian), https://doi.org/10.22034/jtae.2024.8.4.3.

[23] A. R. Fazlyab, F. Fani Saberi, and M. Kabganian, "Fault-tolerant attitude control of the satellite in the presence of simultaneous actuator and sensor faults," *Scientific Reports*, vol. 13, no. 1, 2023, Art. no. 20802, https://doi.org/10.1038/s41598-023-48243-w.

[24] L. Zhao, Z. Lu, W. Liao, T. Liu, K. Ling, and K. Zheng, "Fault-tolerant control for satellite autonomous rendezvous with quality characteristics and actuator uncertainties," *Aerospace Science and Technology*, vol. 150, 2024, Art. no. 109182, https://doi.org/10.1016/j.ast.2024.109182.

[25] M. Leomanni, G. Bianchini, A. Garulli, and A. Giannitrapani, "State feedback control in equinoctial variables for orbit phasing applications," *Journal of Guidance, Control, and Dynamics*, vol. 41, no. 8, pp. 1815-1822, 2018. https://doi.org/10.2514/1.G003402.

[26] M. Leomanni, G. Bianchini, A. Garulli, A. Giannitrapani, and R. Quartullo, "Orbit control techniques for space debris removal missions using electric propulsion," *Journal of Guidance, Control, and Dynamics*, vol. 43, no. 7, pp. 1259-1268, 2020, https://doi.org/10.2514/1.G004735.

[27] A. Garulli, A. Giannitrapani, M. Leomanni, and F. Scortecci, "Autonomous low-Earth-orbit station-keeping with electric propulsion," *Journal of Guidance, Control, and Dynamics*, vol. 34, no. 6, pp. 1683-1693, 2011, https://doi.org/10.2514/1.52985.

[28] E. Jahanbazi, F. Jahangiri, and M. R. Mohammadi, "Neural network based fault tolerant LQR control for orbital maneuvering in LEO satellites using Hall effect thrusters," *AUT Journal of Modeling and Simulation*, vol. 55, no. 1, pp. 171-182, 2023, https://doi.org/10.22060/miscj.2023.22482.5326.

[29] M. F. Shehzad, A. B. Asghar, M. H. Jaffery, K. Naveed, and Z. Čonka, "Neuro-fuzzy system based proportional derivative gain optimized attitude control of CubeSat under LEO perturbations," *Heliyon*, vol. 9, no. 10, 2023, Art. no. e20434, https://doi.org/10.1016/j.heliyon.2023.e20434.

8. APPENDIX

Explicit Form of the State-Space Matrices Aand B

In this appendix, the explicit formulations of the state-space matrices A and B employed in (4) are provided for completeness and reproducibility. These matrices are adopted from [26] and describe the linearized dynamics of the satellite orbital motion expressed in terms of mean orbital elements.

A. State Matrix A

The state matrix $\mathrm{A}(O)$can be expressed as the summation of two components accounting for the dominant environmental perturbations, namely atmospheric drag and gravitational perturbations due to the nonsphericity of the central body, as:

$$\mathbf{A} = \mathbf{A_g(O)} + \mathbf{A_d(O)}.$$

These matrices appear in the set of ordinary differential equations governing the temporal evolution of the mean orbital elements and play a crucial role in accurately modeling long-term orbital behavior.

A.1. Atmospheric Drag Matrix $\mathbf{A}_{\boldsymbol{d}}(\boldsymbol{O})$

The matrix $\mathrm{A}_d(O)$ models the effect of atmospheric drag on the variation of orbital elements such as the semi-major axis, eccentricity components, and inclination. It is expressed as:

$$\mathbf{A}_d(O) = \frac{A}{m} C_D \rho \begin{pmatrix} a_{d_{11}} & 0 & 0 & 0 & 0 & 0 \\ a_{d_{21}} & a_{d_{22}} & 0 & 0 & 0 & a_{d_{26}} \\ a_{d_{31}} & 0 & a_{d_{33}} & 0 & 0 & a_{d_{36}} \\ 0 & 0 & 0 & 0 & 0 & 0 \\ 0 & 0 & 0 & 0 & 0 & 0 \\ 0 & 0 & 0 & 0 & 0 & 0 \end{pmatrix},$$

Where the nonzero elements are defined as

$$a_{d_{11}} = \frac{-1}{2a_R}\sqrt{\frac{\mu}{a}}, \quad a_{d_{21}} = \frac{1}{2} n(e_x + \cos u) a_R,$$

$$a_{d_{22}} = a_{d_{33}} = -\sqrt{\frac{\mu}{a}}, \quad a_{d_{22}} = \sqrt{\frac{\mu}{a}} \sin u,$$

$$d_{d_{31}} \equiv \frac{1}{2} n(e_y + \sin u) a_R, \quad a_{d_{36}} = \sqrt{\frac{\mu}{a}} \cos u.$$

Here, μ denotes the gravitational parameter of the Earth, a is the semi-major axis, n is the mean motion, e_x and e_y are the components of the eccentricity vector, $u$represents the argument of latitude, A/m is the area-to-mass ratio, C_D is the drag coefficient, ρdenotes the atmospheric density, and a_R is the radial acceleration component.

A.2. Gravitational Perturbation Matrix $\mathbf{A}_{\boldsymbol{g}}(\boldsymbol{O})$

The matrix $\mathrm{A}_g(O)$ accounts for gravitational perturbations arising from the oblateness of the Earth, primarily characterized by the J_2 coefficient. This perturbation induces secular and long-period variations in the orbital elements, including nodal regression and apsidal rotation. The matrix is given by:

$$\mathbf{A_g(O)} = \frac{3}{4}\left(\frac{R_E}{a}\right)^2 \frac{nJ_2}{(1-e^2)^2} \begin{pmatrix} 0 & 0 & 0 & 0 & 0 & 0 \\ a_{g_{21}} & a_{g_{22}} & a_{g_{23}} & a_{g_{24}} & 0 & 0 \\ a_{g_{31}} & a_{g_{32}} & a_{g_{33}} & a_{g_{34}} & 0 & 0 \\ 0 & 0 & 0 & 0 & 0 & 0 \\ a_{g_{51}} & a_{g_{52}} & a_{g_{53}} & a_{g_{54}} & 0 & 0 \\ a_{g_{61}} & a_{g_{62}} & a_{g_{63}} & a_{g_{g64}} & 0 & 0 \end{pmatrix} - \begin{pmatrix} 0 & \cdot\cdot & 0 \\ \vdots & \ddots & \vdots \\ \vdots & \vdots & \ddots \\ (3n/2a)a_R & \ldots & 0 \end{pmatrix}$$

The nonzero elements in the above matrix are defined as:

$$a_{g_{21}} = \frac{7a_R}{a}(5\cos^2 i - 1)e_y,$$

$$a_{g_{22}} = -\frac{4(5\cos^2 i - 1)}{(1-e^2)}e_x e_y,$$

$$a_{g_{23}} = -(5\cos^2 i - 1)\Big[\frac{4e_y^2}{(1-e^2)}+1\Big],$$

$$a_{g_{24}} = 10e_y \sin i \cos i,$$

$$a_{g_{31}} = -\frac{7a_R}{2a}(5\cos^2 i - 1)e_x,$$

$$a_{g_{32}} = (5\cos^2 i - 1)\Big[\frac{4e_x^2}{(1-e^2)}+1\Big],$$

$$a_{g_{33}} = \frac{4(5\cos^2 i - 1)}{(1-e^2)}e_x e_y, a_{g_{34}} = -10e_x \sin i \cos i,$$

$$a_{g_{51}} = \frac{7a_R \cos i}{a \sin i_R}, a_{g_{52}} = -\frac{8e_x \cos i}{(1-e^2)\sin i_R},$$

$$a_{g_{53}} = -\frac{8e_y \cos i}{(1-e^2)\sin i_R}, a_{g_{54}} = \frac{2\sin i}{\sin i_R},$$

$$a_{g_{61}} = -\frac{7a_R}{2a}[5\cos^2 i - 1 + (3\cos^2 i - 1)\sqrt{1-e^2}],$$

$$a_{g_{62}} = \frac{e_x}{(1-e^2)}[4(5\cos^2 i - 1) + 3(3\cos^2 i - 1)\sqrt{1-e^2}],$$

$$a_{g_{63}} = \frac{e_y}{(1-e^2)}[4(5\cos^2 i - 1) + 3(3\cos^2 i - 1)\sqrt{1-e^2}].$$

Accordingly, the complete state matrix $A(O)$ incorporates the dominant drag and gravitational perturbations affecting the orbital motion and enables accurate prediction of the long-term evolution of the orbital elements.

B. Control Input Matrix $B(O)$

The control input matrix $B(O)$ represents the influence of control accelerations generated by the Hall-effect thruster on the system states. This matrix is obtained by computing the partial derivatives of the equations of motion with respect to the control inputs. According to [26], the matrix $B(O)$ is given by:

$$\mathbf{B}(O) = \frac{1}{n\Delta t}\begin{pmatrix} 0 & 2 & 0 \\ \sin u & 2\cos u & 0 \\ -\cos u & 2\sin u & 0 \\ 0 & 0 & \cos u \\ 0 & 0 & \sin u \\ -2 & 0 & -\frac{\sin u}{\tan i} \end{pmatrix}.$$

Where Δt denotes the discretization time step, which is typically selected as $\Delta t = 1\text{s}$. The matrix $B(O)$ enables the incorporation of low-thrust control inputs into the linearized orbital dynamics framework and serves as the basis for controller synthesis and orbital transfer optimization.